NANO LETTERS

Letter

pubs.acs.org/NanoLett

Storage and Effective Migration of Li-Ion for Defected β-$LiFePO_4$ Phase Nanocrystals

Hua Guo,[†] Xiaohe Song,[†] Zengqing Zhuo,[†,§] Jiangtao Hu,[†] Tongchao Liu,[†] Yandong Duan,[†] Jiaxin Zheng,[*,†] Zonghai Chen,[‡] Wanli Yang,[§] Khalil Amine,[†,‡] and Feng Pan[*,†]

[†]School of Advanced Materials, Peking University, Shenzhen Graduate School, Shenzhen 518055, People's Republic of China

[‡]Electrochemical Technology Program, Chemical Sciences and Engineering Division, Argonne National Laboratory, Argonne, Illinois 60439, United States

[§]Advanced Light Source, Lawrence Berkeley National Laboratory, Berkeley, California 94720, United States

Supporting Information

ABSTRACT: Lithium iron phosphate, a widely used cathode material, crystallizes typically in olivine-type phase, α-$LiFePO_4$ (αLFP). However, the new phase β-$LiFePO_4$ (βLFP), which can be transformed from αLFP under high temperature and pressure, is originally almost electrochemically inactive with no capacity for Li-ion battery, because the Li-ions are stored in the tetrahedral [LiO_4] with very high activation barrier for migration and the one-dimensional (1D) migration channels for Li-ion diffusion in αLFP disappear, while the Fe ions in the β-phase are oriented similar to the 1D arrangement instead. In this work, using experimental studies combined with density functional theory calculations, we demonstrate that βLFP can be activated with creation of effective paths of Li-ion migration by optimized disordering. Thus, the new phase of βLFP cathode achieved a capacity of 128 mAh g^{-1} at a rate of 0.1 C (1C = 170 mA g^{-1}) with extraordinary cycling performance that 94.5% of the initial capacity retains after 1000 cycles at 1 C. The activation mechanism can be attributed to that the induced disorder (such as $Fe_{Li}Li_{Fe}$ antisite defects, crystal distortion, and amorphous domains) creates new lithium migration passages, which free the captive stored lithium atoms and facilitate their intercalation/deintercalation from the cathode. Such materials activated by disorder are promising candidate cathodes for lithium batteries, and the related mechanism of storage and effective migration of Li-ions also provides new clues for future design of disordered-electrode materials with high capacity and high energy density.

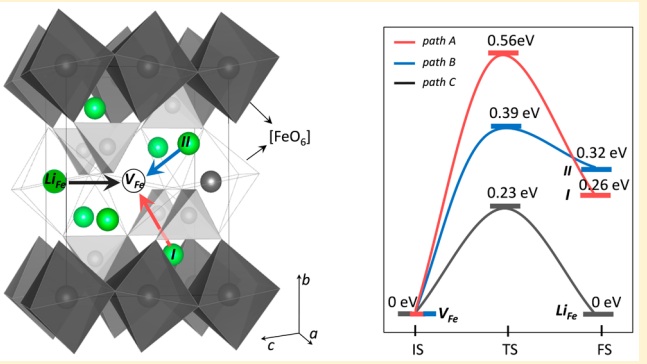

KEYWORDS: *β-$LiFePO_4$, disorder, activation, density functional theory, lithium migration passages*

The rechargeable lithium-ion battery (LIBs) is one of the most popular energy storage devices on the market and is being developed for hybrid electric vehicles and all-electric vehicles. The cathode material of lithium iron phosphate ($LiFePO_4$) is known for safety, environmental friendliness, and high capacity (theoretical capacity of 170 mAh g^{-1}). It is thus considered one of the most promising cathode materials and already widely used in commercial batteries.[1,2]

Lithium iron phosphate typically has an olivine-type structure with space group of *Pmnb,* named α-$LiFePO_4$ (αLFP), which has one-dimensional (1D) channels along the [010] direction for lithium diffusion.[3−5] To improve the electrochemical performance of αLFP (mainly its electronic and ionic conductivity) much work[6−19] has focused on synthesis, modification of morphology, carbon and ionic coating, doping, phase transition, capacity fading mechanism, and influence of defects on the structure. According to theoretical calculations, the 1D migration channels should facilitate the Li-ion diffusion owing to a low activation barrier of 0.27 eV.[20] The theoretical Li-ion diffusion coefficient of αLFP is ~10^{-8} cm^2 s^{-1}. However, its ionic conductivity would be greatly reduced by the defects (or disorder) in the olivine crystal,[20,21] because the defects would block the 1D migration channel and raise the activation barrier for Li-ion diffusion. This also restricts the application to low-temperature synthesis methods, which are low cost but introduce defects easily.

Different from the olivine structure, another phase of lithium iron phosphate, named β-$LiFePO_4$ (βLFP), has a space group of *Cmcm* and higher mass density. It was discovered about two decades ago and was synthesized under high pressure.[22,23] The formation energy of βLFP is smaller than that of αLFP, making it an intermediate and metastable state,[24] and the phase transformation from βLFP to αLFP usually happens when the temperature is increased to about 475 °C.[25] While the Li ion in

Received: October 22, 2015
Revised: November 19, 2015

DOI: 10.1021/acs.nanolett.5b04302
Nano Lett. XXXX, XXX, XXX−XXX

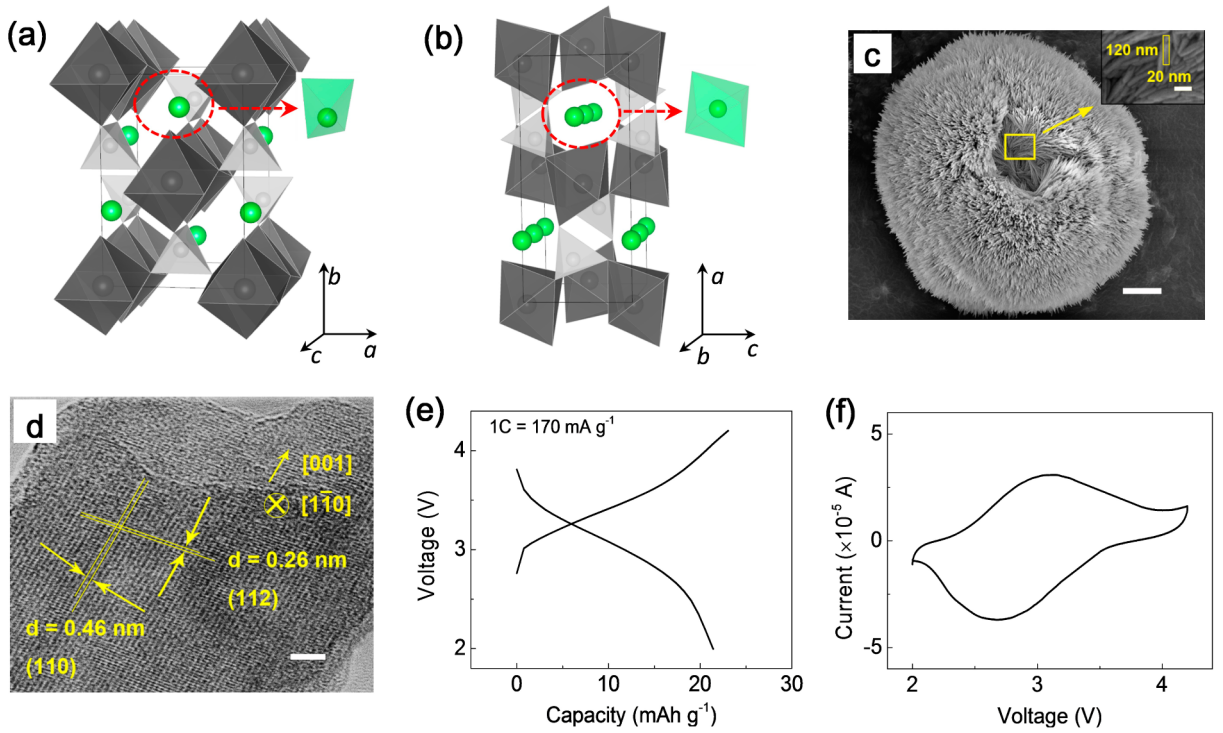

Figure 1. Schematics for structures of βLFP (a) and αLFP (b), and morphology of synthesized βLFP. Lithium ion is shown in green, [FeO_6] octahedron is shown in dark gray, [PO_4] tetrahedron is shown in light gray, and [LiO_4] tetrahedron for βLFP and [LiO_6] octahedron for αLFP is shown in light green. (c) Scanning electron microscopy (SEM) of βLFP. Scale bar, 1 μm. The inset illustrates the size of an individual nanorod. Scale bar, 50 nm. (d) High-resolution transition electron microscopy (HRTEM) of βLFP with (110) and (112) crystal planes marked. (e) Charge/discharge profiles and (f) CV curves of βLFPC-0.

olivine-structured αLFP is octahedral [LiO_6], the βLFP is tetrahedral coordinated, and tetrahedral [LiO_4] ions share a corner with the nearest octahedral [FeO_6] and a corner with the nearest tetrahedral [PO_4] (Figure 1a,b). As a result, the 1D migration channels for Li-ion diffusion in αLFP along the *b*-axis direction disappear in the β phase in which the Fe ion in the octahedral [FeO_6] is oriented similar to the 1D arrangement along the *c*-axis instead. The Li ions in βLFP stay in a captive state and are surrounded by octahedral [FeO_6] and tetrahedral [PO_4]. As a result, the Li ions almost cannot migrate from inside of the crystal to surfaces because of the very long diffusion distance between two adjacent Li-ion sites and very high energy barriers for lithium migration.[26] Previous experimental studies also proved that βLFP exhibits almost no electrochemical activation with low capacity (10−20 mAh g^{-1}, which was attributed to the small amount of residual αLFP[25]). As a consequence, βLFP has not been pursued as a cathode material for LIBs.[25,27]

Here we report a simple method to activate βLFP by introducing disorder (such as $Fe_{Li}Li_{Fe}$ antisite defects, crystal distortion, and amorphous domains) into the structure and creating new lithium migration passages. A high capacity of 128 mAh g^{-1} at a rate of 0.1 C (17 mA g^{-1}) is obtained in this activated materials with extraordinary cycling performance of no obvious capacity fading (retaining more than 94% of initial capacity) after 1000 cycles at 1 C and high rate performance of 65 mAh g^{-1} at 10 C (1.7 A g^{-1}). Further experimental tests and density functional theory (DFT) calculations were employed to get insight of the mechanism on how the storage and effective migration of Li-ions in βLFP created by optimized disordering for the electrochemical activation.

Experimental Methods. *Synthesis of Nanocrystals of Beta Lithium Iron Phosphate.* Nanocrystals of beta lithium iron phosphate were synthesized by a solvothermal method. Precursor was made by mixing ethylene glycol solution of ferrous sulfate and phosphoric acid under an Ar atmosphere, then adding lithium hydroxide solution by drop under stirring. The resulting dark green gel was transferred into a Teflon autoclave under Ar environment. Reaction for 8 h at 180 °C resulted in green nanocrystals of βLFP, which was collected by washing with ethanol and water, and dried in a 80 °C vacuum oven overnight.

Treatment for Controlled Disorder. The as-made nanocrystals of βLFP were mixed with a type of conductive carbon (acetylene black carbon with mean sizes of about 40 nm), then ball milled with zirconia balls at 350 rpm for different times in a zirconia vessel. As a result, the βLFP nanocrystals would closely stick with the conductive carbon.

Characterizations of Materials. Powder X-ray diffraction (XRD) was carried out on a Bruker D8-Advantage powder diffractometer using Cu−Kα radiation from 2θ = 10−120° at 1 s per step of 0.02°. Morphology of the samples was determined by field-emission scanning electron microscopy (SEM, ZEISS SURPA 55) operated at 5 kV and transmission electronic microscopy (TEM, FEI G^2 F30). X-ray photoelectron spectra (XPS) were obtained by using ESCALAB 250Xi. Soft X-ray absorption spectra (XAS) were obtained at the undulator Beamline 8.0.1 of the Advanced Light Source (ALS) at Lawrence Berkeley National Laboratory (LBNL). Elemental analysis was carried out by inductively coupled plasma-atomic emission spectroscopy (ICP-AES, JY2000-2).

Electrochemical Properties Characterization. For coin-cell tests, cathodes were prepared by coating aluminum foil (2 cm^2)

DOI: 10.1021/acs.nanolett.5b04302
Nano Lett. XXXX, XXX, XXX−XXX

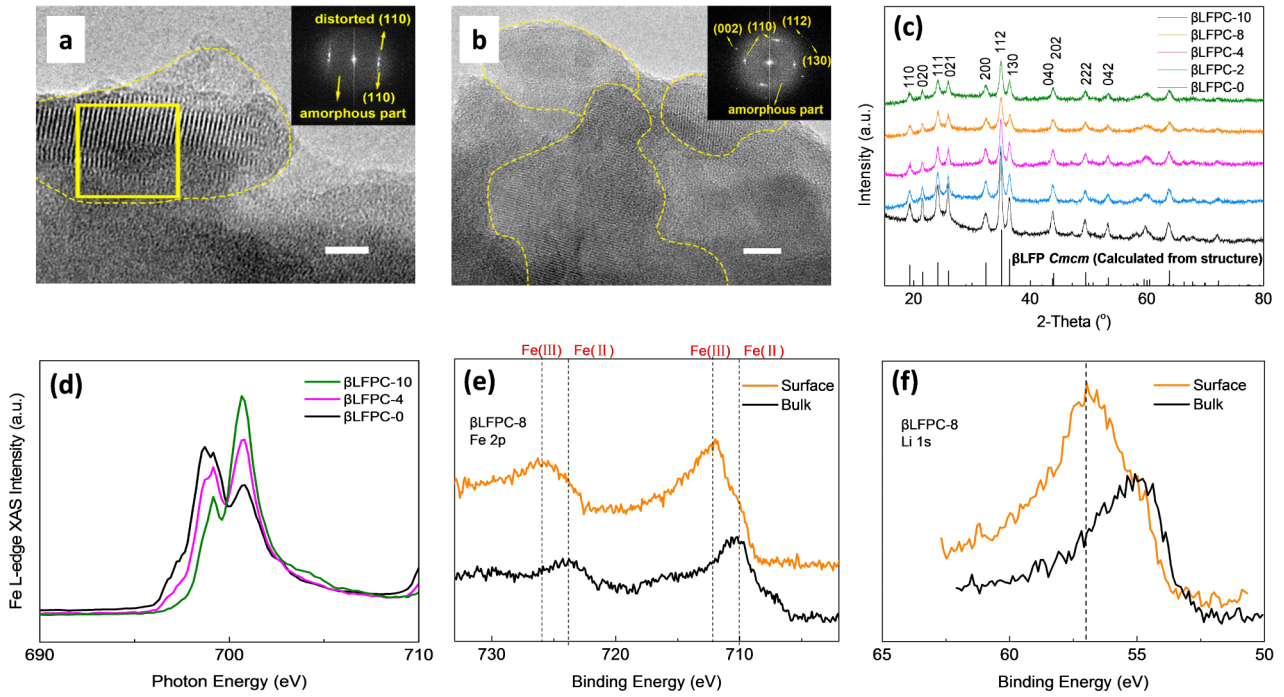

Figure 2. Morphology of ball-milled sample *β*LFPC-8 and characters illustrating partial lithium migrating to carbon during ball-milling. (a) HRTEM of *β*LFPC-8 illustrating the partially distorted domain. Inset shows the fast Fourier transform results of the selected region marked with a yellow box. Scale bar, 3 nm. (b) HRTEM of *β*LFPC-8 showing ordered domains and disordered domains. Inset shows the fast Fourier transform results of whole region. Scale bar, 4 nm. (c) X-ray diffraction results of ball-milled samples *β*LFPC-*n*. (d) Soft X-ray absorption spectra of *β*LFPC-*n* (n = 0, 2, and 10) illustrating that Fe^{2+} (around 698.5 eV) changes to Fe^{3+} (around 701.5 eV) after ball-milling. (e) XPS of milled *β*LFPC-8. Fe is bivalent in bulk (measured with different etching time) while trivalent in the surface. (f) Li_1s XPS spectra of *β*LFPC-8 with peak of 57 eV belonging to Li_xC demonstrating that partial lithium (surface region mostly) was extracted and resided in the covered carbon.

with a slurry of *β*LFP, polyvinylidene fluoride, and acetylene carbon black with thickness of 20 μm in a total weight of 2 mg at a ratio of 50:15:35. This material was dried at 80 °C in a vacuum oven overnight, cut into circles, and assembled in a lithium coin cell. Cyclic voltammetry (CV) was carried out using an electrochemical workstation (ParStat 2273). The capacity of *β*LFPC-*n* (where *n* is the ball-milling time in hours) was calculated to take into account that of the ball-milled conductive carbon [Section S1 in Supporting Information].

Theoretical Calculations. All calculations are performed with the Vienna ab initio simulation package (VASP), using the plane-wave projector-augmented wave method[28] with an energy cutoff of 450 eV. The Perdew–Burke–Ernzerhof (PBE)[29] form of the generalized gradient approximation (GGA) was chosen as the exchange-correlation potential. Considering the strong on-site Coulomb interaction (U) present in the localized 3d electrons of Fe, the PBE+U approach[30] is employed with the same U value of 5.3 eV[31] for $LiFePO_4$ and $FePO_4$. To obtain reliable optimized structures and the total energy all the atomic positions and cell parameters are fully relaxed by use of a conjugate gradient algorithm, and optimized structures are assumed to be reached when the force on each atom is smaller than 0.03 eV/Å. A 2 × 1 × 2 *k*-point grid within the Monkhorst–Pack scheme is used to sample the Brillouin zone of the 2*a* × 2*b* × 2*c* supercell. The climbing-image nudged elastic band (cNEB) method[32] was chosen to calculate the energy barriers for Li-ion diffusion in the bulk $LiFePO_4$, performed in the 2 × 1 × 2 supercell.

Results and Discussion. *Synthesis and Characterization of βLFP Nanocrystals.* The XRD patterns of the fresh *β*LFP nanocrystals synthesized by the solvothermal method are shown in Supporting Information Figure S1. The structure is found to be *β*LFP with the orthorhombic *Cmcm* space group. Lattice parameters are calculated to be a = 5.627 Å, b = 8.366 Å, and c = 6.219 Å from Rietveld refinement, which are in good agreement with our calculated values from density functional theory (DFT) calculations and those in the literatures[25,27] (Supporting Information Table S1). Figure 1c,d exhibits SEM and high-resolution TEM images of the fresh material. As illustrated in Figure 1c, the synthesized *β*LFP nanoparticles form a spiky ball with a 3D porous microstructure. The particles exhibit a size distribution of 4–6 μm. Each individual particle is composed of self-assembled nanocrystals with dimensions of 20 × 20 × 120 nm^3. The TEM image shows the crystalline pattern of a nanorod clearly (Figure 1d). The 120 nm long side is in the [001] direction, and the other two sides (width of 20 nm) are in the [100] and [010] directions. The (110) and (112) crystal planes are also labeled.

Electrochemical Performance of Fresh βLFP Nanocrystal Samples. The fresh *β*LFP nanocrystal samples were mixed with conductive carbon (named as *β*LFPC-0) and investigated in a standard half-cell configuration. The initial capacity is 21 mAh g^{-1} at a rate of 0.1 C (Figure 1e), where the method to calculate the capacity is described in Section S1 of the Supporting Information. In a previous report, the capacity of the prepared *β*LFP sample was attributed to the small amount of residual *α*LFP.[25] However, this explanation does not account for the obtained capacity of *β*LFPC-0 in Figure 1e. First, an XRD analysis did not detect any *α*LFP in our sample (Supporting Information Figure S1). Second, the redox peaks of *β*LFPC-0 appear around 2.9 V in the cyclic voltammogram (CV) curves (Figure 1f), corresponding to redox couple of

DOI: 10.1021/acs.nanolett.5b04302
Nano Lett. XXXX, XXX, XXX–XXX

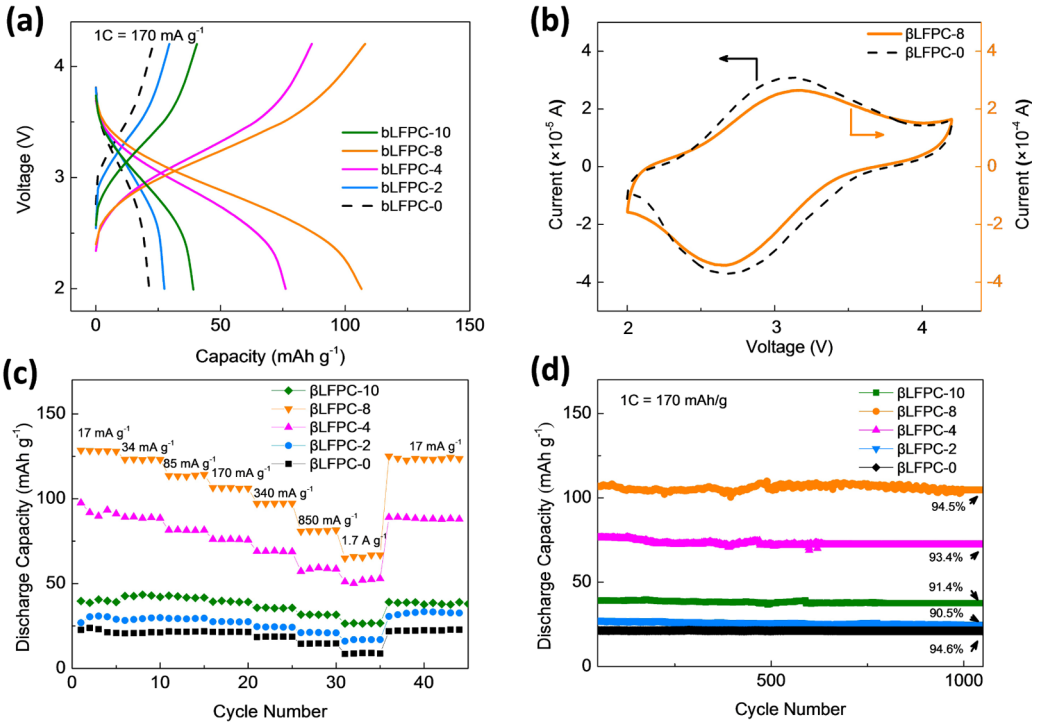

Figure 3. (a) Charge/discharge profiles of samples with ball-milling time of 2 h (*β*LFPC-2), 4 h (*β*LFPC-4), 8 h (*β*LFPC-8), and 10 h (*β*LFPC-10), respectively, compared with *β*LFPC-0. (b) CV curves of *β*LFPC-8 (shown as yellow solid line), compared with *β*LFPC-0 (shown as black dash line). (c) Rate capability and (d) cycling performance of *β*LFPC-*n*..

Fe^{2+}/Fe^{3+}. This voltage is much smaller than the typical value of 3.5 V for *α*LFP. Finally, the slope of the capacity−voltage curves of *β*LFPC-0 (Figure 1e) do not show the typical plateau of *α*LFP at about 3.5 V, similar to the behavior of solid solution materials, such as layered $LiNi_xMn_yCo_zO_2$, with a single phase change during insertion/extraction of lithium.[33] We concluded that the synthesized *β*LFP nanocrystalline materials have no *α*LFP impurity phase and the capacity of our *β*LFPC-0 sample may arise from the large amounts of Li-storage sites near the surface areas from which Li-ions can migrate effectively due to the large surface area of the nanosized particles with various defects formed during the synthesis, as previously reported.[34]

Structure Characterization of Ball-Milled Materials. Ball-milling technique is applied to *β*LFPC-0 and the *n* hours ball-milled materials are named as *β*LFPC-*n*. As shown in Figure 2c, the intensity of the XRD peaks decreases with increasing ball-milling time, indicating that the degree of crystallinity decreases gradually with ball-milling time. Further SEM and TEM measurements show that the fresh *β*LFP particles made up of assembled rod-like nanocrystals are disassembled into nanoparticles with particle size of about 20 × 20 × 30 nm^3 after ball-milling (Supporting Information Figure S2e,f). The HRTEM indicates that crystalline parts with ordered and disordered domains and amorphous domains coexist within an individual ball-milled nanoparticle (Figure 2a,b). Also, lattice distortion is detected in the transition area between the crystalline ordered and disordered areas (Figure 2a). In general, formation of lattice distortion can relax the heavy strain energy generated by the large mismatch between the crystalline ordered and disordered domains, which are induced by ball-milling for the various times. Apart from the lattice crystal distortion, a large share of the amorphous domains can also be seen in the HRTEM image (Figure 2b). The ratio of crystalline parts in different samples could be estimated according to the ratio of the peak area because of their linear relationship.[35,36] The calculated peak area of Figure 2c is shown in Supporting Information Table S2; the ratio of the crystalline parts in *β*LFPC-*n* decrease while the amorphous parts increase gradually as the ball-milling time increased from 0 to 10 h, which is also supported by DSC data[35,36] in Supporting Information Figure S3 where the corresponding temperature of the endothermic peak increase as the ratio of the amorphous parts increasing. The crystalline parts in *β*LFPC-8 are estimated to be more than 50% and hence the amorphous parts less than 50%.

Interestingly, both soft X-ray absorption spectra (XAS) (Figure 2d) and X-ray photoelectron spectroscopy (XPS) analyses (Figure 2e and Supporting Information Figure S5) detect Fe^{3+} in the outer parts of the *β*LFPC-8 sample, indicating that some Li ions are extracted out during the ball-milling process with the conductive carbon. However, the elemental ratios Li/Fe/P for both *β*LFPC-0 and *β*LFPC-8 samples remain almost 1:1:1 according to the inductively coupled plasma-atomic emission spectroscopy (ICP-AES) (Supporting Information Table S6), indicating that the total elemental content of Li does not change in the ball-milled samples. Li_1s XPS spectra of *β*LFPC-8 (Figure 2f) exhibit peaks belonging to Li_xC, indicating that Li ions reside in the surface carbon. From these results, we conclude that Li ions are extracted from *β*LFP nanocrystals to migrate to the conductive carbon and reside in the surface carbon after the ball-milling treatments, which is similar to that the cathode and anode particles contact with each other to create charging process. Thus, a closer carbon contact around the *β*LFP nanoparticles is induced and can enhance electrochemical performance. Furthermore, it can be found that the capacity-voltage curves in the first cycle of *β*LFPC-*n* are asymmetric. The first charging process exhibits a much lower capacity than the subsequent

DOI: 10.1021/acs.nanolett.5b04302
Nano Lett. XXXX, XXX, XXX−XXX

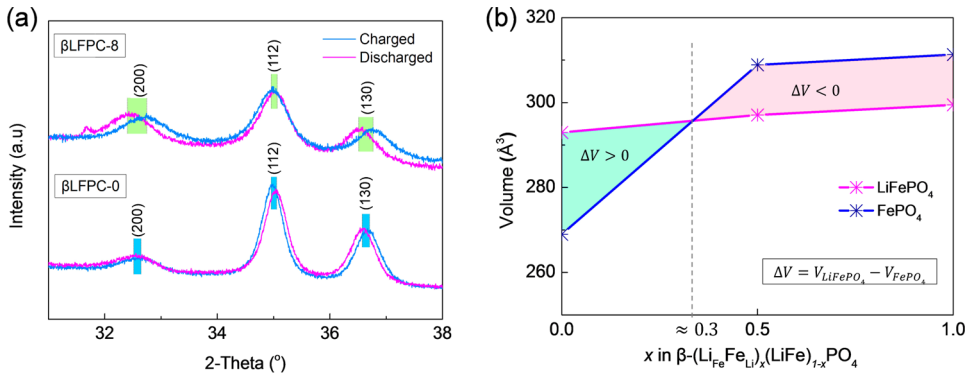

Figure 4. (a) Comparison of XRD peak drift from the charged to discharged states between βLFPC-8 and βLFPC-0. (b) Volume change of lithiated ($LiFePO_4$) and delithiated ($FePO_4$) states as a function of the content of antisite defect $Li_{Fe}Fe_{Li}$.

reversible capacity if we first charge the prepared sample (case A) (Supporting Information Figure S6a), and so does the first discharging process if we first discharge the prepared sample (case B) (Supporting Information Figure S6b). This finding indicates that ball-milling induces Li ions extraction and lowers the capacity at the first charge capacity in case A and the discharge capacity in case B. However, the sum of the first charge capacity and the first discharge capacity is approximately equal to the subsequent reversible capacity after the second charge−discharge cycle.

Significantly Improved Electrochemical Performance by Ball Milling. As shown in the charge/discharge profiles in Figure 3a, increasing the ball milling time of βLFPC-*n* improved the electrochemical performance. βLFPC-8 shows the best electrochemical performance: a capacity of 128, 81 and 65 mAh g^{-1} at rates of 0.1, 5, and 10 C, respectively (1 C = 170 mA g^{-1}) (Figure 3c). Our electrochemical impedance spectra also indicate better electrochemical activity of βLFPC-8 compared with βLFPC-0 (Supporting Information Figure S7). It should be noticed that the samples, especially βLFPC-8, exhibit extraordinary cycling performances with 94.5% of the initial capacity after 1000 cycles at the 1 C rate) (Figure 3d). The CV curves in Figure 3b are similar to those of βLFPC-0 with reduction and oxidation peaks at around 2.9 V (Figure 3b). The broad CV redox peaks are to a certain extent attributed to the amorphous parts and the capacitance characteristics of the ball-milled carbon black (Supporting Information Figure S8). The sloping charge/discharge curves do not keep with the features of materials with 1D lithium passage such as αLFP, which has an obvious plateau. While it is much similar to cathode materials with 2D lithium passages such as the layered $Li[Ni_xCo_yMn_{1-x-y}]O_2$[33] or cathode materials with 3D lithium passages such as spinel $LiMn_2O_4$[37] and cation-disordered materials.[38]

The amorphous domain formed in ball-milling treatment is detected by the HRTEM tests (Figure 2a,b). It has been reported that amorphous $LiFePO_4$ permits insertion/extraction of Li ions and has good volumetric tolerance.[39] It is also supported by our theoretical calculations that the amorphous structure benefits Li ion migration because the redistribution of the FeO_n polyhedrons and the PO_4 tetrahedrons results in much more space to create new migration passages for the imprisoned Li ions (Supporting Information Table S5 and Figure S9). However, βLFPC-10 (10 h ball-milling) exhibits less capacity and poorer electrochemical performances compared to that of βLFPC-8 (8 h ball-milling) sample, although it is expected to have more amorphous content and better carbon-material contact. It means that neither amorphous part nor carbon contact is the key factor for the greatly improved electrochemical property after ball-milling. Moreover, if the amorphous content contributes to the main capacity, the extraordinary cycling performance for the βLFPC-8 cannot be explained, because the typical amorphous LFP has a bad cycling performance and usually survives barely 100 cycles.[40,41] Quantitatively, as what has been discussed in the previous section that the crystalline parts in βLFPC-8 are estimated to be more than 50% and the amorphous parts less than 50%, the amorphous parts could contribute no more than 85 mAh (i.e., 0.5 g × 170 mAh g^{-1}) in per gram of βLFPC-8, and thus the crystalline parts contribute more than 43 mAh (i.e., 128 mAh-85 mAh) in per gram of βLFPC-8 considering capacity of 128 mAh g^{-1}. Therefore, the crystalline parts in βLFPC-8 are active and have a capacity of more than 86 mAh g^{-1}. Further XRD analysis is discussed in the following section.

XRD Analysis Demonstrating the Activation of the Crystalline Part in βLFP. Supporting Information Table S3 lists the fitting lattice parameters of βLFPC-0 and βLFPC-8 according to the XRD patterns. These results indicate that lattices *a* and *b* decrease while *c* increases as the samples evolve from the charged to discharged state. This result is consistent with the trend derived from DFT-calculated lattice parameters, which show that *a* and *b* decrease while c increases when βLFP is charged to β-$FePO_4$ (βFPO). In βLFP, the (200) and (130) planes are parallel with the Fe chains in the *c* direction, the interplanar spacing of (200) depends on *a*, and the interplanar spacing of (130) depends on both *a* and *b*. However, the (112) plane intersects with the *c* axis, and its interplanar spacing depends mainly on *c*. Because the change of lattice parameters *a* and *b* is large while the change of *c* is small, the changes in the interplanar spaces of (200) and (130) should be accordingly larger than that of (112). This finding is in line with the XRD results that peak drifts of (200) and (130) are remarkable while that of (112) is not obvious (Figure 4a). The agreement of the XRD results with the theoretical analysis demonstrates that the lattice parameters change during the charge/discharge cycling. These changes suggest that the crystalline parts of the βLFP-*n* samples are activated to permit extraction/insertion of Li ions.

Another interesting discovery is that the volumetric change ratio per cycle are 0.81 and 1.37% for βLFPC-0 and βLFPC-8, respectively, which are much smaller than the theoretical value of 8.00%. The small volumetric change is reasonable for βLFPC-0 because of its low capacity. While the question remains why the βLFPC-8, which has the highest capacity (about 128 mAh g^{-1}) of all the samples, has such a small

DOI: 10.1021/acs.nanolett.5b04302
Nano Lett. XXXX, XXX, XXX−XXX

volumetric change degree compared with the theoretical value. Further XRD analysis demonstrates that $Fe_{Li}Li_{Fe}$ antisite defects (Supporting Information Table S4) are detected experimentally after the ball-milling. A most likely cause of $Fe_{Li}Li_{Fe}$ maybe that the extraction of Li ions during the ball-milling process would induce the Fe atoms to migrate to Li vacancy sites and thus forming $Fe_{Li}Li_{Fe}$ and V_{Fe} (Fe vacancies). The following DFT study demonstrates that $Fe_{Li}Li_{Fe}$ could significantly decrease the volumetric change of βLFP and activate the βLFP.

A DFT Study of the Dependency Relationship between $Fe_{Li}Li_{Fe}$ Antisite Defects and Volume. On the basis of the above results, we studied the volumetric change as a function of the content of $Fe_{Li}Li_{Fe}$ (Figure 4b). Our calculations demonstrate that $Fe_{Li}Li_{Fe}$ antisite defects are energetically favorable, and they tend to cluster (details in Sections S2 and S3 in Supporting Information). The system with $Fe_{Li}Li_{Fe}$ antisite defects can be represented as β-$(Li_{Fe}Fe_{Li})_x(LiFe)_{1-x}PO_4$, where x indicates the content of $Fe_{Li}Li_{Fe}$. As x increases from 0 to 1, the parameters a and b increase and c decreases for β-$(Fe_{Li})_xFe_{1-x}PO_4$ while a, b, and c remain almost constant for β-$(Li_{Fe}Fe_{Li})_x(LiFe)_{1-x}PO_4$ (Supporting Information Figure S12). If x is in the range of 0 to 0.3, variations of a, b, and c between β-$(Li_{Fe}Fe_{Li})_x(LiFe)_{1-x}PO_4$ and β-$(Fe_{Li})_xFe_{1-x}PO_4$ all decrease. Meanwhile, the volumetric variation between β-$(Li_{Fe}Fe_{Li})_x(LiFe)_{1-x}PO_4$ and β-$(Fe_{Li})_xFe_{1-x}PO_4$ decreases from 8% at x = 0 to about 0% at x = 0.3. When x is larger than 0.3, the volume of delithiated β-$(Fe_{Li})_x(Fe)_{1-x}PO_4$ becomes larger than that of lithiated β-$(Li_{Fe}Fe_{Li})_x(LiFe)_{1-x}PO_4$. This volumetric change is contrary to that of ordered βLFP. Therefore, the $Fe_{Li}Li_{Fe}$ antisite defects weaken the volumetric change between lithiated and delithiated states in the range of 0 to 0.3. Thus, the small volumetric change could be partly attributed to the $Fe_{Li}Li_{Fe}$ antisite defects.

A DFT Study of Li-Ion Migration in Pure and Defective βLFP. For every Li ion in βLFP, there are two kinds of adjacent Li ions. As shown in Figure 5a, one is Li ion A adjacent to Li ion B, with the path A−B connected with a red arrow, and the other is the Li ion A adjacent to Li ion C, with the path A−C in the *ac* plane marked by a blue arrow. The activation barriers are calculated to be 1.2 and 1.4 eV for a Li vacancy to migrate to the adjacent Li sites in the A−B and A−C paths, respectively (Figure 5b).These activation barriers are about 5 times higher than that of αLFP (0.27 eV),[20] so that Li ion migration is forbidden. Hence, theoretical results indicate that ordered βLFP is inactive, which is consistent with previous experimental reports[23,25] and our experimental results.

The most common disorders in βLFP are point defects such as Fe_{Li} (Fe at Li site) or V_{Fe} (Fe site vacancy). When a Fe site is occupied by a Li_{Fe} or V_{Fe}, there are two kinds of newly generated Li migration paths, denoted as Li^{I}−V_{Fe} (path A) and Li^{II}−V_{Fe} (path B), respectively (denoted with red and blue arrows in Figure 5c). In addition, when two adjacent Fe atoms are replaced by two Li_{Fe} or V_{Fe}, a new kind of passage Li_{Fe}−V_{Fe} (path C) forms (denoted with black arrow in Figure 5c). The calculated energy barriers for paths A, B, and C are 0.56, 0.39, and 0.23 eV, respectively (Figure 5d), much lower than the 1.2 eV for ordered βLFP. Thus, defects such as Li_{Fe} or V_{Fe} activate βLFP by creating new Li migration passages with low energy barriers.

On the basis of above discussions, we propose a disorder (such as $Fe_{Li}Li_{Fe}$ antisite defects, crystal distortion, and amorphous domains) collaborative model to reasonably explain the Li-ion migration mechanism in the activated ball-milled samples (Figure 6). In this model, the defective and amorphous domains activate Li-ion effective migration from the storage of the tetrahedral $[LiO_4]$ with low activation barrier, so that Li

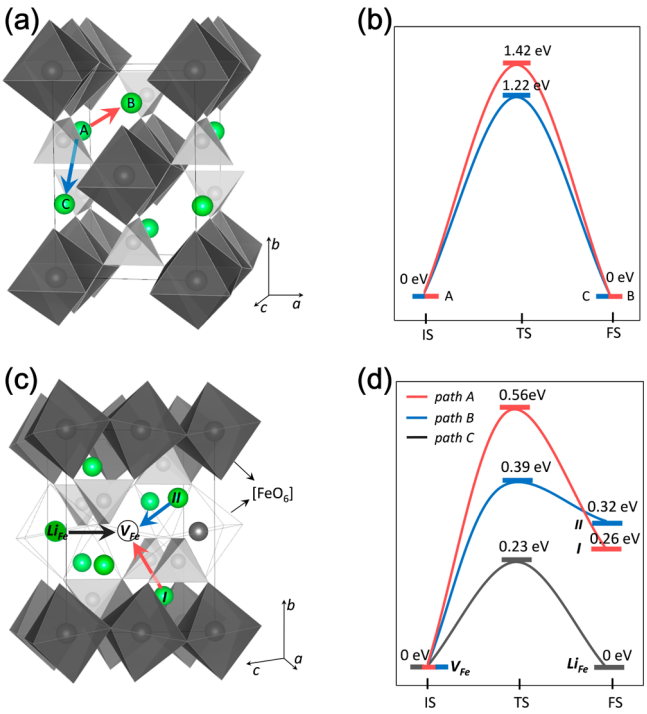

Figure 5. (a) Illustration of two kinds of Li-ion connections in βLFP. Li ion A has adjacent Li ion B on the side, and adjacent Li ion C is up or below A. The connection A−B and A−C are marked with red and blue arrows, respectively. (b) The energy barriers for the hopping of a Li-vacancy along the path A−B (red line) and the path A−C (blue line). IS, TS, and FS represent the initial, final, and transitional states, respectively. (c) Illustration of the three kinds of newly generated Li-ion migration passages in the defective domain. Path A: migration passage for the adjacent Li^{I} when a V_{Fe} is present, marked with the red arrow. Path B: migration passage for the adjacent Li^{II} when a V_{Fe} is present, marked with the blue arrow. Path C: generated when a Li_{Fe} is adjacent to a V_{Fe}, marked with black arrow. (d) The corresponding energy barriers for Li vacancy hopping along the three kinds of newly generated Li-ion migration passages.

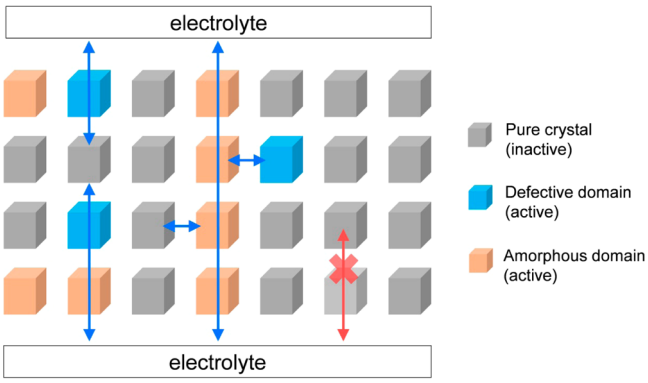

Figure 6. Schematic illustration of the defects/amorphism collaborative model. The gray cube denotes the pure crystal, the blue cube denotes the defective domain, and the yellow cube denotes the amorphous domain. The blue arrows represent the active lithium ion passages, while the red arrow with X means that lithium ion migration is forbidden.

DOI: 10.1021/acs.nanolett.5b04302
Nano Lett. XXXX, XXX, XXX−XXX

ions near the interface of pure crystalline domains can be extracted through activated defective or amorphous domains due to the nanosurface effects. Once these defective and amorphous domains are linked to generate an optimized network, the Li ions will migrate easily from the inner parts to the surface of nanoparticles and then to the electrolyte. As a result, the βLFPC-n (such as βLFPC-8) can achieve a excellent electrochemical performance.

Conclusion. In summary, we synthesize βLFP and activate it with greatly improved electrochemical performance by introducing disorder into the structure. The optimized ball-milled material achieved a high capacity of about 128 mAh g^{-1} at a rate of 0.1 C and a high cycling stability to retain 94.5% of the initial capacity after 1000 cycles at the 1 C (170 mA g^{-1}). Using experimental tests combined with DFT calculations, it is demonstrated that the disorder introduced by the ball-milling, such as defects (Li_{Fe}, Fe_{Li}, and V_{Fe}) in the residual crystalline parts, crystal distortion, and amorphous domains, can create effective Li-ion migration passages, which free the captive stored lithium and facilitate their intercalation/deintercalation from the cathode, thus to activate the βLFP. Such fundamental understanding of Li-ion storage and effective migration would enable the design of disordered-electrode materials with high capacity and high energy density.

■ ASSOCIATED CONTENT

Supporting Information

The Supporting Information is available free of charge on the ACS Publications website at DOI: 10.1021/acs.nanolett.5b04302.

Calculation method for effective capacity and more experimental details of the ball-milled materials, more DFT calculation details about the $Fe_{Li}Li_{Fe}$ antisite defects, X-ray diffraction results, electrochemical impedance spectra. (PDF)

■ AUTHOR INFORMATION

Corresponding Authors

*E-mail: zhengjx@pkusz.edu.cn.
*E-mail: panfeng@pkusz.edu.cn.

Author Contributions

H.G. and X.S. contributed equally to this work.

Notes

The authors declare no competing financial interest.

■ ACKNOWLEDGMENTS

The research was financially supported by Guangdong Innovation Team Project (No. 2013N080), ShenZhen Peacock Plan (Grant KYPT20141016105435850), and Shenzhen Science and Technology Research Grant (Nos. ZDSY20130331145131323, JCYJ20140903101633318, and JCYJ20140903101617271). Additionally, we acknowledge the support of ShenZhen National Super Computing Center.

■ REFERENCES

(1) Padhi, A. K.; Nanjundaswamy, K.; Goodenough, J. *J. Electrochem. Soc.* **1997**, *144*, 1188−1194.
(2) Wang, Y.; He, P.; Zhou, H. *Energy Environ. Sci.* **2011**, *4*, 805−817.
(3) Malik, R.; Abdellahi, A.; Ceder, G. *J. Electrochem. Soc.* **2013**, *160*, A3179−A3197.
(4) Maxisch, T.; Zhou, F.; Ceder, G. *Phys. Rev. B: Condens. Matter Mater. Phys.* **2006**, *73*, 104301.
(5) Nishimura, S.-i.; Kobayashi, G.; Ohoyama, K.; Kanno, R.; Yashima, M.; Yamada, A. *Nat. Mater.* **2008**, *7*, 707−711.
(6) Ellis, B.; Kan, W. H.; Makahnouk, W.; Nazar, L. *J. Mater. Chem.* **2007**, *17*, 3248−3254.
(7) Gu, M.; Shi, W.; Zheng, J.; Yan, P.; Zhang, J.-g.; Wang, C. *Appl. Phys. Lett.* **2015**, *106*, 203902.
(8) Herle, P. S.; Ellis, B.; Coombs, N.; Nazar, L. *Nat. Mater.* **2004**, *3*, 147−152.
(9) Lee, K. T.; Kan, W. H.; Nazar, L. F. *J. Am. Chem. Soc.* **2009**, *131*, 6044−6045.
(10) Liu, H.; Strobridge, F. C.; Borkiewicz, O. J.; Wiaderek, K. M.; Chapman, K. W.; Chupas, P. J.; Grey, C. P. *Science* **2014**, *344*, 1252817.
(11) Love, C. T.; Korovina, A.; Patridge, C. J.; Swider-Lyons, K. E.; Twigg, M. E.; Ramaker, D. E. *J. Electrochem. Soc.* **2013**, *160*, A3153−A3161.
(12) Park, K.-Y.; Park, I.; Kim, H.; Lim, H.-d.; Hong, J.; Kim, J.; Kang, K. *Chem. Mater.* **2014**, *26*, 5345−5351.
(13) Ravnsbæk, D.; Xiang, K.; Xing, W.; Borkiewicz, O.; Wiaderek, K.; Gionet, P.; Chapman, K.; Chupas, P.; Chiang, Y.-M. *Nano Lett.* **2014**, *14*, 1484−1491.
(14) Rui, X.; Zhao, X.; Lu, Z.; Tan, H.; Sim, D.; Hng, H. H.; Yazami, R.; Lim, T. M.; Yan, Q. *ACS Nano* **2013**, *7*, 5637−5646.
(15) Sasaki, T.; Ukyo, Y.; Novák, P. *Nat. Mater.* **2013**, *12*, 569−575.
(16) Song, M.-S.; Kang, Y.-M.; Kim, Y.-I.; Park, K.-S.; Kwon, H.-S. *Inorg. Chem.* **2009**, *48*, 8271−8275.
(17) Wang, L.; He, X.; Sun, W.; Wang, J.; Li, Y.; Fan, S. *Nano Lett.* **2012**, *12*, 5632−5636.
(18) Zhao, Y.; Peng, L.; Liu, B.; Yu, G. *Nano Lett.* **2014**, *14*, 2849−2853.
(19) Zhu, C.; Gu, L.; Suo, L.; Popovic, J.; Li, H.; Ikuhara, Y.; Maier, J. *Adv. Funct. Mater.* **2014**, *24*, 312−318.
(20) Dathar, G. K. P.; Sheppard, D.; Stevenson, K. J.; Henkelman, G. *Chem. Mater.* **2011**, *23*, 4032−4037.
(21) Malik, R.; Burch, D.; Bazant, M.; Ceder, G. *Nano Lett.* **2010**, *10*, 4123−4127.
(22) Amador, U.; Gallardo-Amores, J.; Heymann, G.; Huppertz, H.; Moran, E.; y de Dompablo, M. A. *Solid State Sci.* **2009**, *11*, 343−348.
(23) Garcia-Moreno, O.; Alvarez-Vega, M.; Garcia-Alvarado, F.; Garcia-Jaca, J.; Gallardo-Amores, J.; Sanjuán, M.; Amador, U. *Chem. Mater.* **2001**, *13*, 1570−1576.
(24) Pasternak, M.; Rozenberg, G. K.; Milner, A.; Amanowicz, M.; Zhou, T.; Schwarz, U.; Syassen, K.; Taylor, R. D.; Hanfland, M.; Brister, K. *Phys. Rev. Lett.* **1997**, *79*, 4409.
(25) Zeng, G.; Caputo, R.; Carriazo, D.; Luo, L.; Niederberger, M. *Chem. Mater.* **2013**, *25*, 3399−3407.
(26) Ashton, T. E.; Laveda, J. V.; MacLaren, D. A.; Baker, P. J.; Porch, A.; Jones, M. O.; Corr, S. A. *J. Mater. Chem. A* **2014**, *2*, 6238−6245.
(27) Voß, B.; Nordmann, J. r.; Kockmann, A.; Piezonka, J.; Haase, M.; Taffa, D. H.; Walder, L. *Chem. Mater.* **2012**, *24*, 633−635.
(28) Blöchl, P. E. *Phys. Rev. B: Condens. Matter Mater. Phys.* **1994**, *50*, 17953.
(29) Perdew, J. P.; Burke, K.; Ernzerhof, M. *Phys. Rev. Lett.* **1996**, *77*, 3865.
(30) Anisimov, V. I.; Zaanen, J.; Andersen, O. K. *Phys. Rev. B: Condens. Matter Mater. Phys.* **1991**, *44*, 943.
(31) Zhou, F.; Marianetti, C.; Cococcioni, M.; Morgan, D.; Ceder, G. *Phys. Rev. B: Condens. Matter Mater. Phys.* **2004**, *69*, 201101.
(32) Henkelman, G.; Uberuaga, B. P.; Jónsson, H. *J. Chem. Phys.* **2000**, *113*, 9901−9904.
(33) Wei, Y.; Zheng, J.; Cui, S.; Song, X.; Su, Y.; Deng, W.; Wu, Z.; Wang, X.; Wang, W.; Rao, M. *J. Am. Chem. Soc.* **2015**, *137*, 8364−8367.
(34) Jensen, K. M.; Christensen, M.; Gunnlaugsson, H. P.; Lock, N.; Bøjesen, E. D.; Proffen, T.; Iversen, B. B. *Chem. Mater.* **2013**, *25*, 2282−2290.
(35) Pan, P.; Liang, Z.; Cao, A.; Inoue, Y. *ACS Appl. Mater. Interfaces* **2009**, *1*, 402−11.

DOI: 10.1021/acs.nanolett.5b04302
Nano Lett. XXXX, XXX, XXX−XXX

(36) Luo, J.; Huang, A. M.; Park, S. H.; Suib, S. L.; O'Young, C. L. *Chem. Mater.* **1998**, *10*, 1561−1568.
(37) Xu, B.; Meng, S. *J. Power Sources* **2010**, *195*, 4971−4976.
(38) Lee, J.; Urban, A.; Li, X.; Su, D.; Hautier, G.; Ceder, G. *Science* **2014**, *343*, 519−522.
(39) Fang, Y.; Xiao, L.; Qian, J.; Ai, X.; Yang, H.; Cao, Y. *Nano Lett.* **2014**, *14*, 3539−3543.
(40) Mathew, V.; Kim, S.; Kang, J.; Gim, J.; Song, J.; Baboo, J. P.; Park, W.; Ahn, D.; Han, J.; Gu, L.; Wang, Y.; Hu, Y.-S.; Sun, Y.-K.; Kim, J. *NPG Asia Mater.* **2014**, *6*, e138.
(41) Kim, S. W.; Ryu, J.; Park, C. B.; Kang, K. *Chem. Commun. (Cambridge, U. K.)* **2010**, *46*, 7409−11.

DOI: 10.1021/acs.nanolett.5b04302
Nano Lett. XXXX, XXX, XXX−XXX